AN APPROACH TO SUBPIXEL ACCURACY WIDENING CRACK WIDTH DETERMINATION IN IMAGE SEQUENCES

F. Liebold, H.-G. Maas

Institute of Photogrammetry and Remote Sensing, Technische Universität Dresden, Germany -
(frank.liebold, hans-gerd.maas)@tu-dresden.de

Technical Commission II

KEY WORDS: Deformation Measurement, Crack Detection, Crack Analysis, Image Sequence Analysis, Digital Image Correlation.

ABSTRACT:

As an extension to existing work on crack detection and subpixel accuracy crack width determination as a tool for civil engineering material testing, the paper shows an algorithmic approach to handle widening cracks with relative rotations between related crack borders. In the first time step under zero-load, a set of points to be tracked through consecutive frames of an image sequence is defined. Then, subpixel-precise displacement fields are computed for the image data of the following time steps using an 8-parameter least-squares matching approach. The points are triangulated into a mesh, and the changes of the inner geometry of the triangles are considered with a mathematical model assuming a split of each triangle. With this model, subpixel-precise deformation vectors are derived. Crack candidates are determined by a thresholding applied to the vectors' lengths. After an estimation of the crack normal, a decomposition of the deformation vectors is applied, allowing to compute crack widths and shear movements. As a novel contribution to the technique, a model extension is proposed for the case of a relative rotation between the crack borders in order to reduce systematic errors. The model includes two separate rigid transformations for each crack side.

1. INTRODUCTION

Crack detection and deformation analysis is an important field in material testing. In opposite to classical instruments such as inductive displacement transducers or strain gauges, image sequence based methods offer a contact-less measurement with high spatial and temporal resolution and they are thus suited for deformation measurement. In the past years, several photogrammetric approaches to crack detection were published: (Fraser and Riedel, 2000) measured displacements of cooling steel beams using a three camera configuration. (Whiteman et al., 2002) determined vertical deflections of artificial targets on concrete beams using a stereo camera system. (Barazzetti and Scaioni, 2009) used a monocular system and an orientation frame to analyze cracks. (Benning et al., 2004, Görtz, 2004, Lange et al., 2006, Lange and Benning, 2006) observed artificial targets on concrete specimens with a trinocular camera system during load tests. They also computed crack widths in 4-point elements (rectangles) without regarding rotations between the states. (Hampel and Maas, 2009) computed dense displacement fields using cross-correlation and least-squares matching and determined crack widths by analyzing discontinuities in profiles through the shift fields along the x and y direction in the image coordinate system. (Barazzetti and Scaioni, 2010) tracked signalized targets in monocular image sequences of the observed concrete beams during load tests. In addition, they applied a Wallis filter for image pre-processing to untargeted surfaces, followed by cross-correlation and least-squares matching to determine displacement fields of interest points. (Geers et al., 1996) presented an algorithm to obtain strain fields from discrete 2D displacement fields. The inclusion of strains matches to the requirements in determining ductile deformations. Moreover, it can also be used to detect cracks. (Koschitzki et al., 2011, Liebold and Maas, 2016) analyzed monocular image sequences. They worked with a triangulation of the points of the displacement field and computed strains to detect cracks. (Liebold and Maas, 2018, Liebold and Maas, 2020) proposed another deformation quantity that allows to derive crack widths in triangular meshes for monocular image sequences with subpixel accuracy. This approach is more suitable for brittle material and can also be used for crack propagation measurements (Liebold et al., 2020a). (Liebold et al., 2019) extended the method to non-planar object surfaces observed with stereo camera image sequences, and (Liebold et al., 2020b) showed how to compute full 3D crack opening vectors from 3D displacement fields.

The paper at hand extends the model of (Liebold and Maas, 2020, Liebold et al., 2020b) in a way that a relative rotation between crack sides is considered. The following section briefly repeats the analysis of monocular image sequences for crack detection and crack width measurement and shows the extension for handling relative rotations of related crack faces. The third section goes into the analysis of multiocular image sequences. The publication closes with a conclusion as well an outlook.

2. CRACK DETECTION BY MONOCULAR IMAGE SEQUENCE ANALYSIS

The procedure starts with the image acquisition. For measurements with monocular camera systems, the following requirements should be fulfilled to avoid systematic errors:

- The object surface to be observed should be planar with an artificial or natural texture suited for image matching.
- The optical axis should be perpendicular to the object's

surface. Alternatively, an inclination should be corrected by an image rectification.

- Out-of-plane movements should be avoided.
- A camera calibration should be done to reduce systematic errors of lens distortion but is often neglected.

The first image of the sequence is recorded under zero-load to be considered as reference image. In this image, a set of points is defined, for instance a regular grid. Fig. 1a shows an image used as reference from a concrete beam in a 4-point bending test determined with a monocular camera system (one half of the beam is shown).

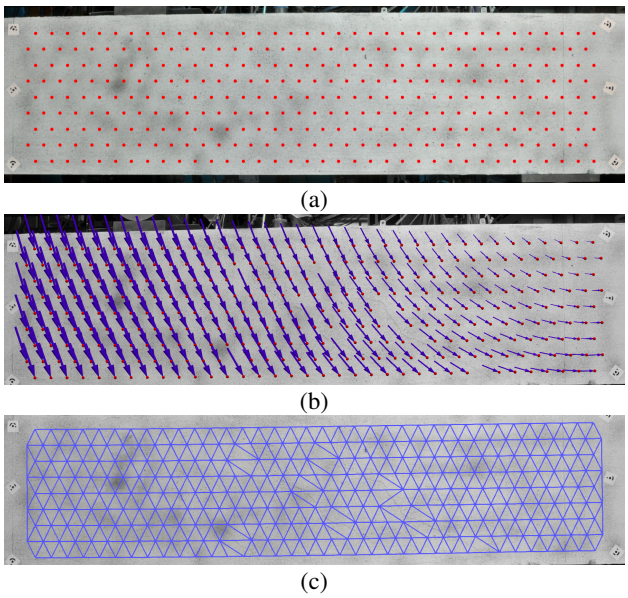

(a) (b) (c)

Figure 1. (a) Reference image with the points to be matched; (b) deformed state and displacement field (scale factor: 5, based on (Liebold et al., 2020a)); (c) mesh of the matching points tracked successfully. Based on (Liebold and Maas, 2018).

2.1 Displacement Vector Field Determination and Triangulation

Then, between the reference and the images of the deformed states, digital image correlation techniques such as cross-correlation and least-squares matching are applied (Ackermann, 1984) for the determination of subpixel-precise shifts for the defined points, see Fig. 1a. Fig. 1b shows an image of a deformed state with the displacement vector field. The points, for which displacements were computed successfully, are triangulated into a triangular mesh, see Fig. 1c. The triangulation is repeated for each further (later) image, due to a different number of successful matchings.

2.2 Deformation Analysis

In the model of the parallel translation, an occuring crack will split a triangle into two parts with one part being shifted (Liebold and Maas, 2020). Thus, for the two vertices on the one side of the crack, a rigid transformation (translation $\vec{t}$, rotation matrix $\mathbf{R}$) is applied and for the remaining vertex on the other crack side, there is an additional relative shift $\vec{t}_{rel}$. Fig. 2 illustrates the schematic split of a triangle with the reference as well as the deformed state. Eq. 1 shows the mathematical formulation with a distinction of cases. For 2D, the set M_1 contains the indices of the base edge vertices b_1 and b_2 whereas M_2 contains the remaining index h. The triangle edge with the smallest length difference is used as base edge (indices b_1 and b_2, Eq. 2).

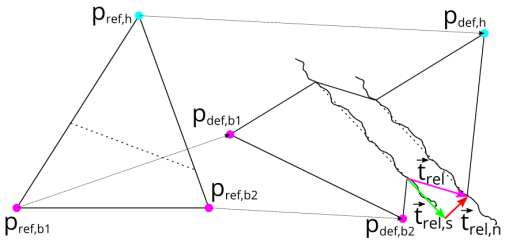

Figure 2. Scheme for the triangle split, reference state on the left, deformed on the right. Based on (Liebold et al., 2019).

$$\vec{p}_{def,i} = \begin{cases} \vec{t} + \mathbf{R} \cdot \vec{p}_{ref,i} & \forall\, i \in M_1 \\ \vec{t} + \mathbf{R} \cdot \vec{p}_{ref,i} + \vec{t}_{rel} & \forall\, i \in M_2 \end{cases} \tag{1}$$

$$b_1, b_2 = \underset{i,j}{argmin} |||| \vec{s}_{def,ij} || - || \vec{s}_{ref,ij} |||| \\ \forall\, (i,j) \in \{(1,2),(1,3),(2,3)\} \tag{2}$$

where $\vec{s}_{ref,ij} = \vec{p}_{ref,j} - \vec{p}_{ref,i}$
$\vec{s}_{def,ij} = \vec{p}_{def,j} - \vec{p}_{def,i}$

To solve Eq. 1, first, $\vec{t}$ and $\mathbf{R}$ are computed with the indices of the base edge vertices. The solution for $\vec{t}_{rel}$ is then computed as follows:

$$\vec{t}_{rel} = \vec{p}_{def,h} - \vec{t} - \mathbf{R} \cdot \vec{p}_{ref,h} \tag{3}$$

$\vec{t}_{rel}$ is used as deformation vector and includes a normal as well as a shear component, see Fig. 2 and Sec. 2.4. The vector's length $||\vec{t}_{rel}||$ is used as a scalar deformation quantity for brittle material. A thresholding is applied to detect deformed triangles (crack candidates). The threshold δ depends on the quality of the displacement field, which often has subpixel precision so that values of 0.1-0.2 px are suitable for δ. The crack position for these deformed triangles is estimated by the weighted average:

$$\vec{m}_{def} = (\vec{p}_{def,b1} + \vec{p}_{def,b2} + 2 \cdot \vec{p}_{def,h})/4 \tag{4}$$

Fig. 3a depicts the deformation vector field for the deformed triangles where $||\vec{t}_{rel}||$ exceeds the threshold δ. Fig. 3b shows a zoom in of the deformation vector field. In Fig. 3c, the color-coded triangle mesh for the values of $||\vec{t}_{rel}||$ is depicted.

2.3 Crack Normal Estimation and 2D Crack Opening Vector

For each crack candidate (deformed triangle), a crack normal vector is estimated as follows: First, the deformed neighbor triangles of the crack candidate are determined. Here, neighbors have at least one common vertex and also second order neighbors (neighbors and neighbors of neighbors) are used. This is followed by a line fit (optionally weighted, see (Liebold and Maas, 2018)) computed with the centers (see Eq. 4) of the crack candidate and its neighbors. The orthogonal to the line is used

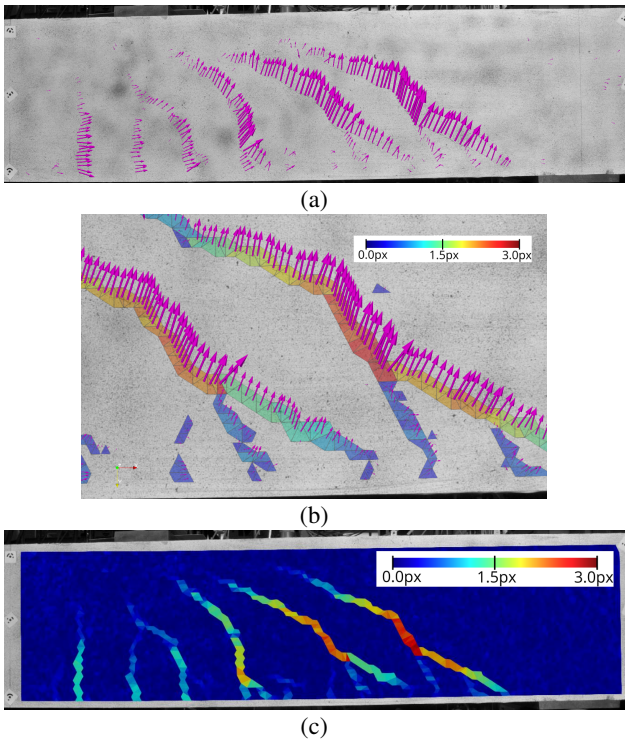

Figure 3. (a) Deformation vector field for the crack candidates (scale factor: 80); (b) zoom in for the deformation vector field (scale factor: 80); (c) color-coded triangular mesh of the scalar values of $||\vec{t}_{rel}||$, based on (Liebold and Maas, 2020).

as an estimation for the crack normal $\vec{n}'$. This vector $\vec{n}'$ is then normalized and it is oriented toward the deformation vector:

$$\text{If } \vec{t}_{rel}^{\,T} \cdot \vec{n}' < 0 : \vec{n} = -\frac{\vec{n}'}{||\vec{n}'||} \text{ otherwise } \vec{n} = \frac{\vec{n}'}{||\vec{n}'||}. \quad (5)$$

Fig. 4a illustrates the principle of the crack normal estimation. Considering this procedure, large triangles may lead to less precise results, and at crack crossings as well at mesh borders, systematic errors may appear.

With the knowledge of the crack normal, $\vec{t}_{rel}$ is decomposed into the normal and the perpendicular shear component, see Eq. 6 as well as Fig. 4b.

$$\vec{t}_{rel,n} = \vec{t}_{rel}^{\,T} \cdot \vec{n} \cdot \vec{n}; \qquad \vec{t}_{rel,s} = \vec{t}_{rel} - \vec{t}_{def,n} \quad (6)$$

The scalar components of the 2D crack opening vectors are the crack width r and the shear s, see Eq. 7. These values are very interesting in material testing.

$$\begin{aligned} r &= ||\vec{t}_{rel,n}|| = \vec{t}_{rel}^{\,T} \cdot \vec{n}; \\ s &= ||\vec{t}_{rel,s}|| = \sqrt{||\vec{t}_{rel}||^2 - r^2} \end{aligned} \quad (7)$$

Fig. 4c depicts the corresponding normal components in red and the shear components in green of the example above.

2.4 Model Extension for Relative Rotations

In case of relative rotations between related crack faces, systematic errors will occur when applying the model with the parallel

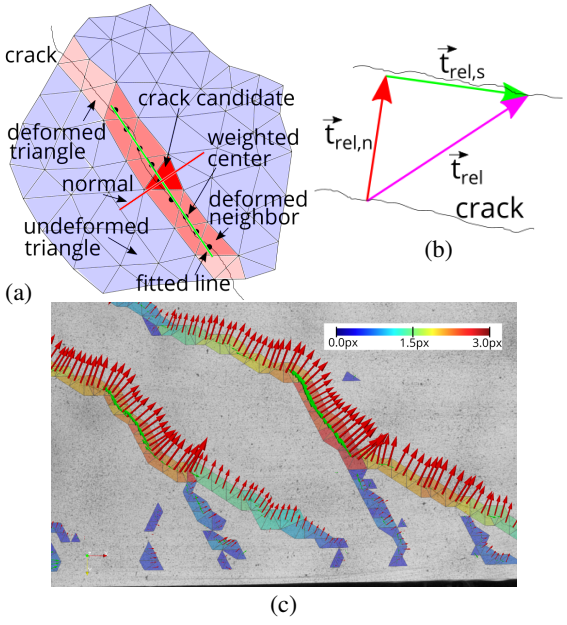

Figure 4. (a) Crack normal estimation, based on (Liebold and Maas, 2018); (b) decomposition of the deformation vector; (c) vector field of the normal (red) and the shear components (green) of the deformation vector (scale factor: 80).

translation (Eq. 1). For such cases, the model can be extended. Fig. 5a illustrates a triangle split with relative shift and rotation. The following computation steps can be performed optionally after the calculations of section 2.2 and are applied to the deformed triangles. The extended model for relative rotations with two separate rigid transformations (translations $\vec{t}_1$ and $\vec{t}_2$, rotation matrices $\mathbf{R}_1$ and $\mathbf{R}_2$) is:

$$\vec{p}_{def,i} = \begin{cases} \vec{t}_1 + \mathbf{R}_1 \cdot \vec{p}_{ref,i} & \forall\, i \in M_1 \\ \vec{t}_2 + \mathbf{R}_2 \cdot \vec{p}_{ref,i} & \forall\, i \in M_2 \end{cases} \quad (8)$$

Now, for M_2, at least two points are required to solve the system of Eq. 8. To extend the set M_2, all undeformed neighbor triangles with the vertex $\vec{p}_{def,h}$ are determined and the remaining vertices are added to M_2. This is visualized in Fig. 5b where the red triangle is a crack candidate, the other soft red triangles are neighboring deformed triangles and the undeformed triangles with $\vec{p}_{def,h}$ are depicted in strong blue. The green vertices are base line points and the yellow vertices belong to M_2.

The deformation vector $\vec{t}_{rel}$ is ambiguous and varies along the crack border. It is not included in Eq. 8 and is computed separately. Here, $\vec{t}_{rel}$ is defined by the difference of the two transformations applied to the crack location (Eq. 10). From the digital image correlation data, the crack position assigned to the triangle (in the reference state) can be estimated as shown in Eq. 9.

$$\vec{m}_{ref} = (\vec{p}_{ref,b1} + \vec{p}_{ref,b2} + 2 \cdot \vec{p}_{ref,h})/4 \quad (9)$$

$$\vec{t}_{rel} = \vec{t}_2 - \vec{t}_1 + (\mathbf{R}_2 - \mathbf{R}_1) \cdot \vec{m}_{ref} \quad (10)$$

Fig. 5c depicts a deformed image of a tension test with relative rotation. It is blended with the color-coded map with the $||\vec{t}_{rel}||$ and the deformation vector field (scale factor: 15) is shown.

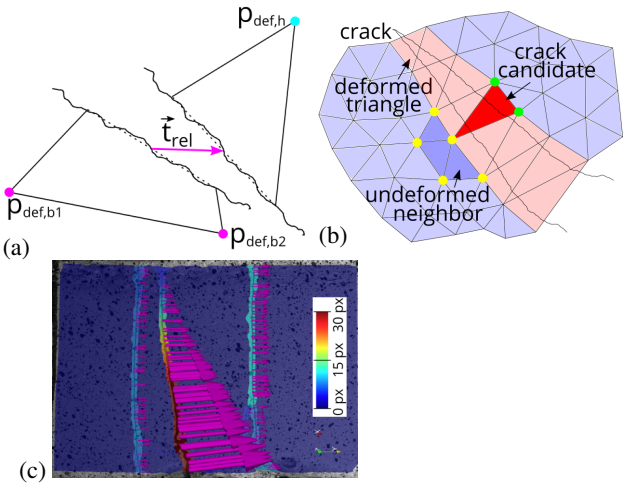

Figure 5. (a) Triangle split with relative shift and relative rotation; (b) vertices of M_1 in green and extended set of vertices M_2 in yellow; (c) color-coded mesh with values of $||\vec{t}_{rel}||$ and deformation vector field (scale factor: 15) of a tension test with a relative rotation.

2.4.1 Error Assessment To evaluate the benefit of the model extension, the error vectors are computed with and without model extension. Assuming that there are two different rigid transformations on each crack side, the target value is:

$$\vec{t}_{rel,target} = \vec{t}_2 - \vec{t}_1 + (\mathbf{R}_2 - \mathbf{R}_1) \cdot \vec{p}_{ref,crack} \qquad (11)$$

The position $\vec{p}_{ref,crack}$ is the exact crack position that is not known. Without model extension, the calculated value from Eq. 3 is expressed as follows:

$$\begin{aligned} \vec{t}_{rel,PT} &= \vec{p}_{def,h} - \vec{t}_1 - \mathbf{R}_1 \cdot \vec{p}_{ref,h} \\ &= \vec{t}_2 - \vec{t}_1 + (\mathbf{R}_2 - \mathbf{R}_1) \cdot \vec{p}_{ref,h} \end{aligned} \qquad (12)$$

Then, the error without model extension (PT: parallel translation) is:

$$\begin{aligned} \vec{\epsilon}_{PT} &= \vec{t}_{rel,PT} - \vec{t}_{rel,target} \\ &= (\mathbf{R}_2 - \mathbf{R}_1) \cdot (\vec{p}_{ref,h} - \vec{p}_{ref,crack}) \end{aligned} \qquad (13)$$

There is still a remaining error in case of the model extension (ME), computed by the difference of Eq. 10 and Eq. 11:

$$\begin{aligned} \vec{\epsilon}_{ME} &= \vec{t}_{rel,ME} - \vec{t}_{rel,target} \\ &= (\mathbf{R}_2 - \mathbf{R}_1) \cdot (\vec{m}_{ref} - \vec{p}_{ref,crack}) \end{aligned} \qquad (14)$$

The relative errors are:

$$\epsilon_{PT,rel} = \frac{||\vec{\epsilon}_{PT}||}{||\vec{t}_{rel,target}||}; \qquad \epsilon_{ME,rel} = \frac{||\vec{\epsilon}_{ME}||}{||\vec{t}_{rel,target}||} \qquad (15)$$

The error vectors depend on the difference of the rotation matrices and on the difference vector of between the exact crack position and the vertex $\vec{p}_{h,ref}$ (model of PT) or the weighted center (Eq. 9, with ME): the smaller the difference vector, the smaller the error.

The errors are also analyzed in a simulation shown in Fig. 6. A grid of points is defined with a horizontal distance of ten units

Table 1. Median absolute and relative errors with and without model extension.

Relative rotation	1°	2°	5°	10°	20°
median($\|\|\vec{\epsilon}_{PT}\|\|$)	0.088	0.18	0.44	0.88	1.75
median($\|\|\vec{\epsilon}_{ME}\|\|$)	0.021	0.042	0.11	0.21	0.42
median($\epsilon_{PT,rel}$)	0.035	0.037	0.038	0.039	0.039
median($\epsilon_{ME,rel}$)	0.0074	0.0077	0.0079	0.0079	0.0079

that is triangulated into a mesh (Fig. 6a). In addition, a line (red) is defined that separates the set of points into two parts where different rigid transformations are applied. The perpendicular foot points (green points) of the triangle center points are used as the target crack positions. The deformed state is visualized in Fig. 6b and c where the error vectors (Eq. 13 for Fig. 6b and Eq. 14 for Fig. 6c) are shown as vector fields (scale factor 10), too. The errors have a preferred direction along the crack and they are reduced if the model extension is used (shorter arrows).

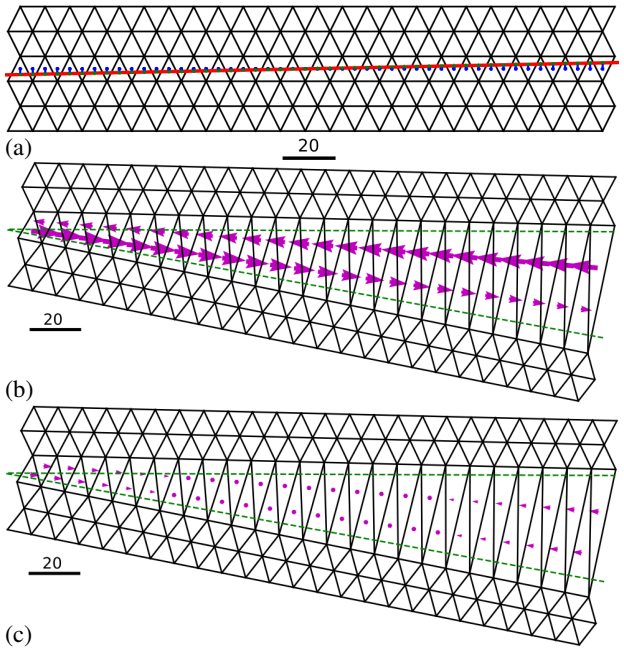

Figure 6. (a) Triangular mesh (reference state) with the red separation line, blue triangle center points and blue connections to the perpendicular foots (green points) on the line; (b) mesh (deformed state) and error vector field for the model of PT (scale factor: 10) for 10° relative rotation; (c) mesh (deformed state) and error vector field for ME (scale factor: 10).

The errors with the ME depend directly on the distances in Fig. 6a (blue connections) and are smaller than without model extension in the most cases. The corresponding boxplots are shown in Fig. 7a; over all relative rotation angles, the error medians are reduced by about 74 % if the ME is used. Fig. 7b depicts the boxplots of the relative errors where the medians stay at a constant level and are reduced by almost 80 % when using the ME, see also Table. 1 (without units).

2.4.2 Practical Test A practical test is done with two printed patterns (Fig. 8, size DIN-A4) that are created using a vector graphics editor. The pattern is separated in two parts by a horizontal line and the upper part is rotated and shifted in the deformed state (Fig. 8b) whereas Fig. 8a shows the reference state. The relative rotation is set to 5°. In the corners of the patterns, there are circular targets for a projective transformation.

Each of the two printed patterns is recorded using a calibrated

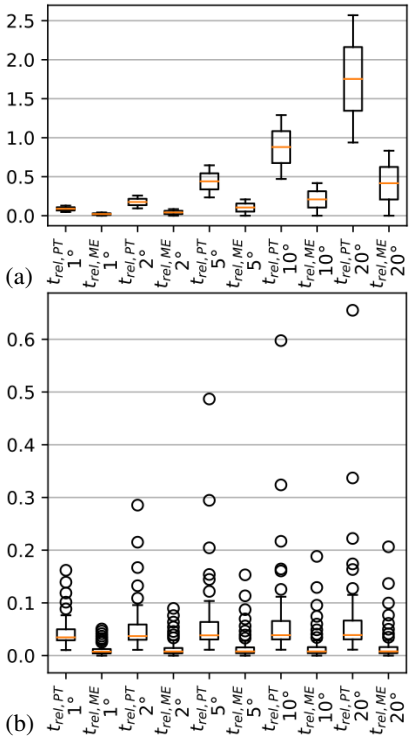

Figure 7. (a) Boxplots of absolute errors (without dimension); (b) boxplots of relative errors for different relative rotation angles.

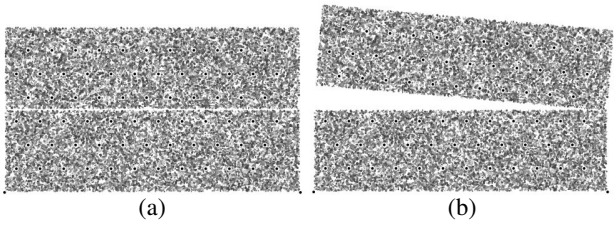

Figure 8. (a) Reference pattern generated with vector graphics; (b) deformed state with a known rotation of 5° of the upper part.

industrial camera (AVT Mako G503B) combined with a lens of 16 mm focal length. The algorithm of section 2.2 is applied to compute the deformation vectors $\vec{t}_{rel,PT}$ (model of parallel translation PT) as well as the vectors $\vec{t}_{rel,ME}$ using the model extension (ME, section 2.4). The subpixel-accurate ellipse measurement of the corner targets and a projective transformation into the coordinate system of the pattern generation is done that allows to compare the results with target values from the pattern generation and also solves the scale problem. In order to obtain the target values, the perpendicular foot points of the triangle centers $\vec{m}_{ref}$ (Eq. 9) of the detected deformed triangles are computed and used as target crack positions. After this, Eq. 11 is applied to calculate the $\vec{t}_{rel,target}$ vectors.

Similar to section 2.4.1, the absolute errors ($||\vec{\epsilon}_{PT}||$ from Eq. 13 and $||\vec{\epsilon}_{ME}||$ from Eq. 14) as well as the relative errors ($\epsilon_{PT,rel}$ and $\epsilon_{ME,rel}$ from Eq. 15) are computed. The corresponding boxplots are shown in Fig. 9. For the relative rotation of 5°, the median of the absolute errors is reduced by 53 % and the median of the relative errors is reduced by 62 % when using the model extension.

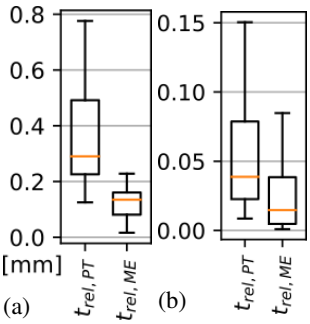

Figure 9. (a) Boxplots of absolute errors; (b) boxplots of relative errors for a relative rotation angle of 5°.

3. CRACK DETECTION BY STEREO IMAGE SEQUENCE ANALYSIS

Compared to crack detection in monocular image sequences, there are less restrictions for the analysis of multiocular image sequences, and it allows to measure non-planar surfaces and out-of-plane displacements. In case of stereo image sequences, a preparation step, the calibration of the stereo camera system, is required to determine the inner and the relative orientation.

3.1 Displacement Vector Field Determination and Triangulation

The first step of data acquisition is recording a first image pair without any deformations of the probe to be observed. In one of the two images, a set of points to be tracked is defined. The corresponding image points in the second image are determined using digital image correlation techniques. For the next recordings of the deformed states, the corresponding points in both images are computed. The scheme in Fig. 10 shows the principle of the determination of the displacement field of the 3D surface points and the triangulation into a mesh.

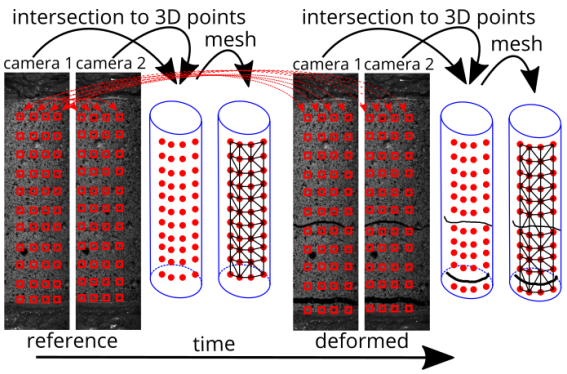

Figure 10. Principle of the displacement field determination and triangulation, based on (Liebold et al., 2019).

3.2 Deformation Analysis

First, deformed triangles are detected by the analysis of the inner geometry done by a congruent mapping to 2D coordinates (Liebold et al., 2020b). In order to do that, the edge vectors of the triangle $\vec{s}_{ref,ij}$ and $\vec{s}_{def,ij}$ are computed as well as the indices of the base edge b_1 and b_2 using Eq. 2. The remaining vertex has the index h.

The congruent mapping is done for the reference as well as the deformed state and is combined with the rigid transformation.

The relevant transformed 2D coordinates of the reference triangle $\vec{q}_{ref,h,t}$ and the deformed triangle $\vec{q}_{def,h}$ are:

$$\begin{aligned}\vec{q}_{ref,h,t} &= \begin{pmatrix} x_{ref,b1,t} + dx_{ref,b1,h} & dy_{ref,b1,h} \end{pmatrix}^T; \\ \vec{q}_{def,h} &= \begin{pmatrix} dx_{def,b1,h} & dy_{def,b1,h} \end{pmatrix}^T \end{aligned} \tag{16}$$

where

$$\begin{aligned} x_{ref,b1,t} &= \tfrac{1}{2} \cdot (||\vec{s}_{def,b1,b2}|| - ||\vec{s}_{ref,b1,b2}||) \\ dx_{ref,b1,h} &= \frac{\vec{s}_{ref,b1,b2}^{\,T} \cdot \vec{s}_{ref,b1,h}}{||\vec{s}_{ref,b1,b2}||} \\ dy_{ref,b1,h} &= \sqrt{||\vec{s}_{ref,b1,h}||^2 - dx_{ref,b1,h}^2} \\ dx_{def,b1,h} &= \frac{\vec{s}_{def,b1,b2}^{\,T} \cdot \vec{s}_{def,b1,h}}{||\vec{s}_{def,b1,b2}||} \\ dy_{def,b1,h} &= \sqrt{||\vec{s}_{def,b1,h}||^2 - dx_{def,b1,h}^2} \end{aligned}$$

From these coordinates, the 2D deformation vector is derived:

$$\vec{t}_{rel,2D} = \vec{q}_{def,h} - \vec{q}_{ref,h,t} \tag{17}$$

The norm of the vector $||\vec{t}_{rel,2D}||$ is used as the deformation quantity in order to detect deformed triangles by thresholding (deformed if $||\vec{t}_{rel,2D}|| > \delta$). Fig. 11a visualizes the principle of the thresholding.

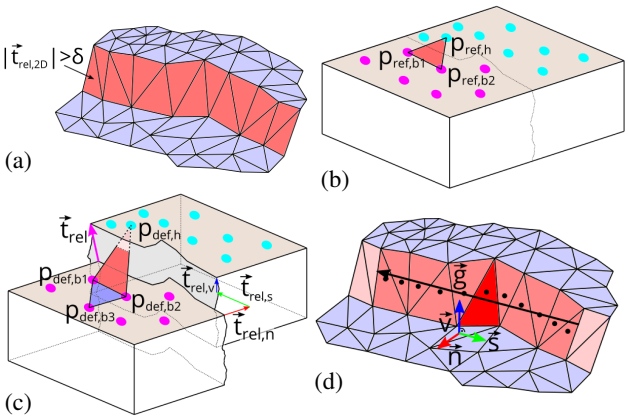

Figure 11. (a) Thresholding applied to $||\vec{t}_{rel,2D}||$ to detect deformed triangles in red whereas undeformed triangles are blue; (b) block before cracking in the reference state; (c) broken block with relative shift of the right half such that the red crack triangle is deformed, the neighboring base triangle is shown in blue; (d) crack direction $\vec{g}$ determination by line fit through neighboring deformed triangles (red) and coordinate system of the crack opening vector derived from $\vec{g}$. Based on (Liebold et al., 2020b).

After this, the model of parallel translation and the mathematical formulation of Eq. 1 is reused for the 3D case and applied to the deformed triangles. To solve Eq. 1 in 3D, M_1 has to contain at least three points so that the three vertices of the triangle are not enough. Further information is needed, at least one additional point around the base edge. The set M_1 is extended by the additional vertex b_3 of the undeformed neighbor triangle having the same edge with the vertices b_1 and b_2: $M_1 = \{b_1, b_2, b_3\}$ and $M_2 = \{h\}$. Fig. 11b shows the reference state whereas Fig. 11c illustrates the deformed state of a broken block. The surface points are separated into two sets (magenta and cyan). The deformed triangle is red and the undeformed neighbor with the common base line is blue that delivers a third vertex (index b_3) for M_1.

In Fig. 12, an analysis of one epoch from a torsion test is shown. Fig. 12a depicts the color-coded mesh with the values of $||\vec{t}_{rel,2D}||$. Fig. 12b visualizes the 3D deformation vectors computed with the model of parallel translation.

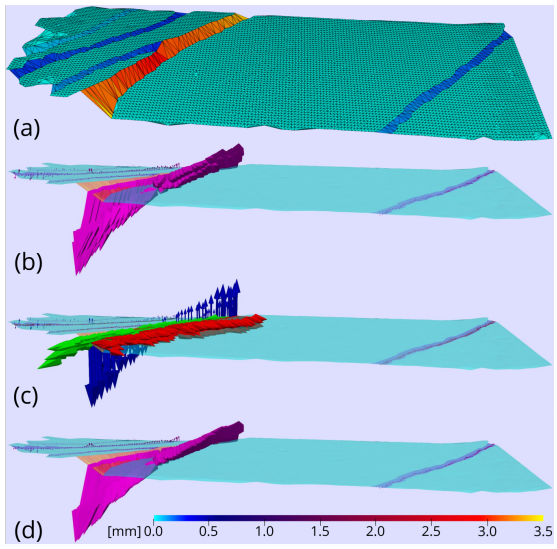

Figure 12. (a) Color-coded mesh of $||\vec{t}_{rel,2D}||$ (deformed state); (b) deformation vectors with the model of parallel translation; (c) decomposition of the deformation vectors to crack normal (red), shear (green), vertical component (blue); (d) deformation vectors with the model extension for relative rotation (scale factor: 5 for (b),(c),(d)).

3.3 3D Crack Opening Vector

Similar to the 2D case, the direction of the crack $\vec{g}$ is estimated first by applying a line fit through the center points of neighboring deformed triangles, as illustrated in Fig. 11d. After computing the vertical direction $\vec{v}$, the vector $\vec{g}$ is used to compute the crack normal $\vec{n}$ as well as the shear direction $\vec{s}$, see Eq. 18.

$$\begin{aligned} \vec{v} &= \frac{(\vec{p}_{b2} - \vec{p}_{b1}) \times (\vec{p}_{b3} - \vec{p}_{b1})}{||(\vec{p}_{b2} - \vec{p}_{b1}) \times (\vec{p}_{b3} - \vec{p}_{b1})||}; \\ \vec{n} &= \frac{\vec{v} \times \vec{g}}{||\vec{v} \times \vec{g}||}; \qquad \vec{s} = \vec{v} \times \vec{n} \end{aligned} \tag{18}$$

The normal ($\vec{t}_{rel,n}$), the shear ($\vec{t}_{rel,s}$) as well as the vertical ($\vec{t}_{rel,v}$) component of the deformation vector are computed by projections:

$$\begin{aligned} \vec{t}_{rel,n} &= \vec{t}_{rel}^{\,T} \cdot \vec{n} \cdot \vec{n}; \\ \vec{t}_{rel,s} &= \vec{t}_{rel}^{\,T} \cdot \vec{s} \cdot \vec{s}; \\ \vec{t}_{rel,v} &= \vec{t}_{rel}^{\,T} \cdot \vec{v} \cdot \vec{v} \end{aligned} \tag{19}$$

Fig. 12c depicts the components of the deformation vectors of the torsion test example (red: crack normal components, green: shear components, blue: vertical components, scale factor: 5). An experimental validation is shown in (Liebold et al., 2020b): They determined a relative accuracy of 0.0002 for $\vec{t}_{rel}$ and 0.0003 for the crack opening vector.

Table 2. Median absolute and relative errors for 3D case.

Relative rotation	1°	2°	5°	10°	20°
median($\|\|\vec{\epsilon}_{PT}\|\|$)	0.087	0.17	0.43	0.86	1.72
median($\|\|\vec{\epsilon}_{ME}\|\|$)	0.027	0.055	0.14	0.27	0.54
median($\epsilon_{PT,rel}$)	0.036	0.039	0.041	0.041	0.041
median($\epsilon_{ME,rel}$)	0.012	0.014	0.015	0.016	0.017

3.4 Model Extension for Relative Rotations

The procedure is similar to section 2.4. It is an optional step after applying the model with parallel translation and is only computed for deformed triangles. The mathematical model in Eq. 8 is reused with 3D coordinates and 3D rotations. To solve this system, for both sets M_1 and M_2, at least three points are required. M_1 already has a cardinality of three in the model of PT but M_2 needs to be extended. This is done in the same way as in 2D. All undeformed neighbor triangles of the vertex $\vec{p}_{def,h}$ are determined, and the vertices of these triangles are added to M_2, as illustrated in Fig. 13 (red bordered cyan circles). After computing the parameters $\vec{t}_1$, $\mathbf{R}_1$, $\vec{t}_2$ and $\mathbf{R}_2$, the deformation vector $\vec{t}_{rel}$ is calculated using Eq. 9 and Eq. 10.

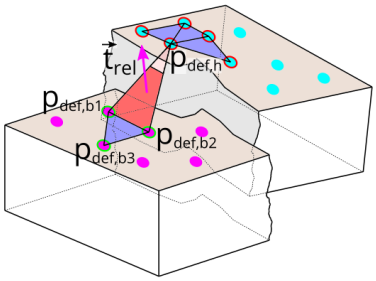

Figure 13. Relative rotation of the right half, neighboring undeformed triangles to $\vec{p}_{def,h}$ in blue with cyan red bordered vertices.

Fig. 12d shows the vector field of the deformation vectors computed with the extended model. Compared to Fig. 12b, the vectors have a less scattering.

3.4.1 Error Assessment The consideration of the 2D case in section 2.4 can be transferred to 3D so that Eq. 11, 13 and 14 are reused here. The errors are also analyzed in a simulation, where a grid of 3D points on a cylinder surface and a separation plane are defined, see Fig. 14a (triangle edge lengths: 15.7, 12.7, 12.7 without units). Target values for the deformation vectors are obtained by projecting the centers of intersected triangles onto the plane and applying Eq. 11. Fig. 14b and c show the deformed state with the error vectors exaggerated with scale factor of 20 for a relative rotation of 10°. In Fig. 15a and b, the boxplots of the absolute and relative error vector lengths are depicted for different relative rotation angles. Tab. 2 shows the medians. The behavior is similar to the 2D case. Also here, the median errors (absolute) are reduced by about 70 % and the medians of relative error decrease by more than 60 %.

3.4.2 Practical Test A practical test is performed with the same pattern as used for the 2D algorithm of Sec. 2.4.2 (Fig. 8). A stereo system of two UI-3280CP Rev.2 cameras with lenses of focal lengths of 25 mm is used to record the patterns. The calibration (inner and relative orientation) of the system is done with the commercial software GOM ARAMIS (Carl Zeiss GOM Metrology GmbH). Ellipse measurements of the circular corner points allow a rigid transformation into the target value system. The target values are calculated in the same way as

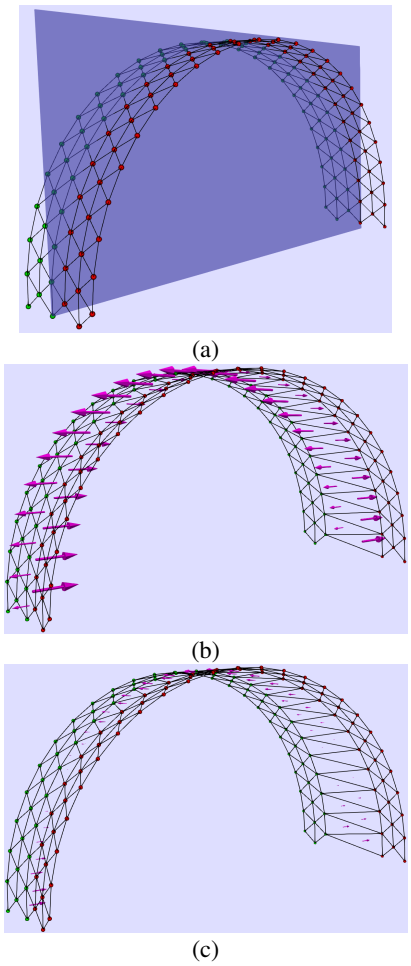

Figure 14. (a) Triangular mesh (reference state) with separation plane (blue), left side with green points and right side with red points; (b) mesh (deformed state) and error vector field for the model of PT (scale factor: 20) for 10° relative rotation; (c) mesh (deformed state) and error vector field for ME (scale factor: 20).

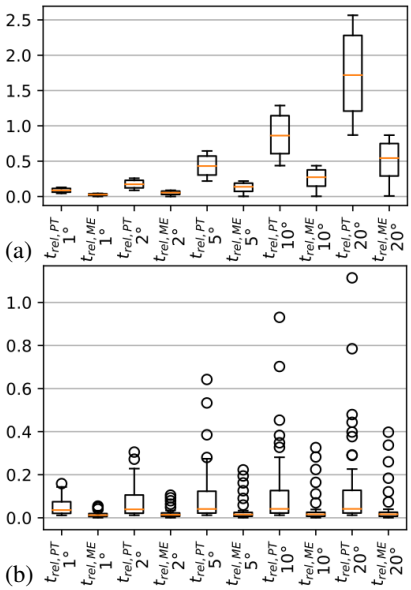

Figure 15. (a) Boxplots of absolute errors; (b) boxplots of relative errors for different relative rotation angles.

in Sec. 2.4.2. Fig. 16 depicts the boxplots of the absolute and relative errors. In the 3D case, the usage of the model extension reduces the median absolute error by 32 % and the median relative error by 26 %.

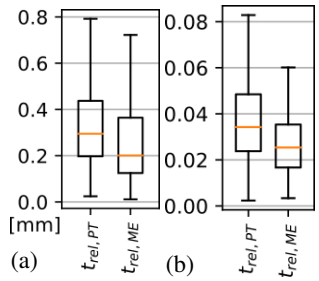

Figure 16. (a) Boxplots of absolute errors; (b) boxplots of relative errors for a relative rotation angle of 5° for 3D case.

4. CONCLUSION AND OUTLOOK

The paper at hand presents a method for subpixel-precise crack analysis based on triangulated displacement fields. The algorithm is suitable for deformation measurements with monocular and multiocular image sequences of load tests with brittle material. For relative rotations between the crack borders, a model extension is proposed that reduces the median error by 60 to 80 % in a simulation. A practical test also shows an error reduction of 26 to 62 %.

Future work could focus on a more precise crack position determination by a combination with other techniques.

ACKNOWLEDGEMENTS

The research work presented in the publication has been funded by the Deutsche Forschungsgemeinschaft (DFG, German Research Foundation–SFB/TRR 280; Projekt-ID: 417002380). Furthermore, we thank the Institute of Construction Materials at TU Dresden and the Institutes of Concrete Structures at TU Dresden and Leibnitz University Hannover as well as the Department of Chemical and Materials Engineering at PUC Rio for providing the data sets.

REFERENCES

Ackermann, F., 1984. Digital Image Correlation: Performance and Potential Application in Photogrammetry. *The Photogrammetric Record*, 11(64), 429–439.

Barazzetti, L., Scaioni, M., 2009. Crack measurement: Development, testing and applications of an automatic image-based algorithm. *ISPRS Journal of Photogrammetry and Remote Sensing*, 64(3), 285–296.

Barazzetti, L., Scaioni, M., 2010. Development and Implementation of Image-based Algorithms for Measurement of Deformations in Material Testing. *Sensors*, 10(8), 7469–7495.

Benning, W., Lange, J., Schwermann, R., Effkemann, C., Görtz, S., 2004. Monitoring crack origin and evolution at concrete elements using photogrammetry. *Int. Arch. Photogramm. Remote Sens. Spatial Inf. Sci.*, XXXV-B5, 678–683.

Fraser, C. S., Riedel, B., 2000. Monitoring the thermal deformation of steel beams via vision metrology. *ISPRS Journal of Photogrammetry and Remote Sensing*, 55(4), 268–276.

Geers, M. G. D., De Borst, R., Brekelmans, W. A. M., 1996. Computing strain fields from discrete displacement fields in 2D-solids. *International Journal of Solids and Structures*, 33(29), 4293–4307.

Görtz, S., 2004. Zum Schubrissverhalten von Stahlbeton- und Spannbetonbalken aus Normal- und Hochleistungsbeton. PhD thesis, RWTH Aachen.

Hampel, U., Maas, H.-G., 2009. Cascaded image analysis for dynamic crack detection in material testing. *ISPRS Journal of Photogrammetry and Remote Sensing*, 64(4), 345–350.

Koschitzki, R., Schacht, G., Schneider, D., Marx, S., Maas, H.-G., 2011. Integration of photogrammetry and acoustic emission analysis for assessing concrete structures during loading tests. *Proceedings of SPIE Optical Metrology*, 8085, International Society for Optics and Photonics.

Lange, J., Benning, W., 2006. Crack detection using photogrammetry. *Proceedings of 9th European Conference on Non-Destructive Testing, Berlin*, BB 103-CD, NDT, German Society for Non-Destructive Testing, 1–8.

Lange, J., Benning, W., Siering, K., 2006. Crack detection at concrete construction units from photogrammetric data using image processing procedures. *Int. Arch. Photogramm. Remote Sens. Spatial Inf. Sci.*, XXXVI-7, 493–496.

Liebold, F., Heravi, A. A., Mosig, O., Curbach, M., Mechtcherine, V., Maas, H.-G., 2020a. Crack Propagation Velocity Determination by High-speed Camera Image Sequence Processing. *Materials*, 13(19).

Liebold, F., Maas, H.-G., 2016. Advanced spatio-temporal filtering techniques for photogrammetric image sequence analysis in civil engineering material testing. *ISPRS Journal of Photogrammetry and Remote Sensing*, 111, 13–21.

Liebold, F., Maas, H.-G., 2018. Sub-pixel accuracy crack width determination on concrete beams in load tests by triangle mesh geometry analysis. *ISPRS Ann. Photogramm. Remote Sens. Spatial Inf. Sci.*, IV-2, 193–200.

Liebold, F., Maas, H.-G., 2020. Strategy for Crack Width Measurement of Multiple Crack Patterns in Civil Engineering Material Testing Using a Monocular Image Sequence Analysis. *PFG – Journal of Photogrammetry, Remote Sensing and Geoinformation Science*, 88(3), 219–238.

Liebold, F., Maas, H.-G., Deutsch, J., 2020b. Photogrammetric determination of 3D crack opening vectors from 3D displacement fields. *ISPRS Journal of Photogrammetry and Remote Sensing*, 164, 1 - 10.

Liebold, F., Maas, H.-G., Heravi, A. A., 2019. Crack Width Measurement for Non-planar Surfaces by Triangle Mesh Analysis in Civil Engineering Material Testing. *Int. Arch. Photogramm. Remote Sens. Spatial Inf. Sci.*, XLII-2/W18, 107–113.

Whiteman, T., Lichti, D., Chandler, I., 2002. Measurement of deflections in concrete beams by close-range digital photogrammetry. *Int. Arch. Photogramm. Remote Sens. Spatial Inf. Sci.*, XXXIV-4.